Journal of Materials Processing Tech. 254 (2018) 52–59

Contents lists available at ScienceDirect

Journal of Materials Processing Tech.

journal homepage: www.elsevier.com/locate/jmatprotec

Development of process efficiency maps for selective laser sintering of polymeric composite powders: Modeling and experimental testing

Fei Shen, Shangqin Yuan, Chee Kai Chua, Kun Zhou*

School of Mechanical and Aerospace Engineering, Nanyang Technological University, Singapore 639798, Singapore

ARTICLE INFO

Keywords:
Additive manufacturing
Selective laser sintering
Process modeling
Polymeric powders
Process efficiency maps

ABSTRACT

This study develops process efficiency maps for selective laser sintering of polymeric composite powders to provide guidance for process parameter optimization via numerical modeling and experimental testing. Specifically, the sintering process for carbon nanotubes-reinforced PA12 nanocomposite powders is modeled to evaluate and predict the temperature distribution and dimensions of their melt pools. The numerical model takes into account the interaction between the laser beam and powder bed, the temperature-dependent material properties and the solid-liquid phase transition. The experimental testing is used to determine the material properties and validate the modeling predictions. The predicted melt pool features are utilized for the development of process efficiency maps that relate the printing productivity and laser energy consumption efficiency to the laser power and scanning speed.

1. Introduction

Selective laser sintering (SLS), one of the powder-based additive manufacturing techniques, offers powerful capacity to fabricate parts with complex geometry through selectively fusing powders layer by layer (Goodridge et al., 2012). The process parameters such as the laser power, laser scanning speed, scanning pattern, hatching space, powder layer thickness and building orientation affect the thermal history of powder layers during the fusion and subsequent solidification, which plays a crucial role in the process efficiency and part quality such as the dimensional accuracy, surface roughness, porosity, microstructure and mechanical behavior (Yadollahi and Shamsaei, 2017).

Experimental investigations have mainly focused on the influences of the process parameters on the quality of built parts. Wang et al. (2007) proposed a neural network approach to study the effects of process parameters on part shrinkage. Sachdeva et al. (2013) used the variance analysis to investigate the effects of process parameters on part surface roughness. A similar method was employed to determine the effects of process parameters on the part density (Fatemi et al., 2017) and hardness (Singh et al., 2017). Caulfield et al. (2007) investigated the influences of the energy density controlled by the laser power, laser beam diameter, hatching space and scanning speed on the physical and mechanical properties of printed parts, and observed that the parts became more isotropic, solid and stronger as the level of the energy density increased. Tan et al. (2016) evaluated the effects of the energy density on the Young's modulus, ultimate strength and dimensional deviation of the printed spiral wound membranes for water treatment.

The effects of powders on the part quality have also been experimentally investigated. Yuan et al. (2016a, b) studied the thermal behavior of the carbon nanotubes (CNTs)-reinforced polyamide 12 (PA12) nanocomposite powders and investigated the effects of CNTs on the microstructures, mechanical behavior of printed parts. It was found that the mechanical strength and elongation of the parts were increased by over 30% due to the reinforcement of CNTs. The CNTs also improved the heat absorption and conductivity capabilities of the composite powders, which was preferable for the laser sintering process. Bai et al. (2017) reported the improved toughness induced by the coating of CNTs on polyamide 11 powders. Therefore, it is worthwhile to investigate nanofillers-reinforced nanocomposite powders and their applications in SLS.

The process efficiency of SLS is another important aspect that should be considered, which is characterized by the printing productivity and the consumption of the laser energy during the sintering process. The printing productivity is determined by the volumetric increment rate of the melt pool. Franco et al. (2010) experimentally investigated the relationship between the dimensions (width and depth) of a sintered track and the energy density. Franco and Romoli (2012) evaluated the printing productivity and the energy consumption based on the measured dimensions. The energy density in the certain range of 0.02–0.08 J/mm^2 for PA12 was recommended for the process efficiency.

Numerical approaches offer great facility to model the sintering

* Corresponding author.
E-mail address: kzhou@ntu.edu.sg (K. Zhou).

https://doi.org/10.1016/j.jmatprotec.2017.11.027
Received 31 July 2017; Received in revised form 12 November 2017; Accepted 16 November 2017

process under different operational parameters. Two methods of the process modeling are classified according to their simulation scales. The first one is the mesoscopic method that considers individual powder particles and the capillary force, gravitational force and wetting of their melt pool. Körner et al. (2011) and Körner et al. (2013) used the two-dimensional lattice Boltzmann model to simulate the sintering of a single layer and multiple layers, respectively. Later, Khairallah and Anderson (2014) developed a three-dimensional mesoscopic model of a single track to simulate the melting and solidification of powders. However, the meso-scale models involve extensive computation cost due to the consideration of powder particles. The other one is the macroscopic method which homogenizes powders as continuum media, which is suitable for the large-scale simulation. Dong et al. (2009) modeled the transient heat transfer during the sintering process with the consideration of the phase transition and the temperature-dependent material properties to evaluate the temperature and density distribution. The laser heat source was modeled as a surface heat distribution on the powder bed, leading to the underestimation of the depth of the melt pool. A more realistic model of the heat source was then developed to consider the transmission of the laser beam into the porous powder bed. Riedlbauer et al. (2014) used the model to predict the dimensions of melt pools and validated the predictions through experimental testing. The effects of the process parameters on the temperature distribution (Peyre et al., 2015) and the dimensions of the melt pool (Foroozmehr et al., 2016) were also numerically investigated.

So far, no systematic researches combining the experimental testing and the process modeling have been conducted on the SLS process efficiency. The experimental studies have mainly focused on the quality of printed parts, but the experimental trial and error process is too time-consuming and costly and may not be affordable. The process modeling is able to provide an insight into the mechanism of the sintering process; however, few numerical works have been conducted to evaluate the process efficiency.

This study aims to investigate the process efficiency for SLS of polymeric composite powders using both numerical modeling and experimental testing. The heat transfer in the sintering of carbon nanotubes-reinforced PA12 nanocomposite powders is modeled to predict the temperature distribution and dimensions of their melt pools, which takes into account the interaction between the laser beam and powder bed, the temperature-dependent material properties and the phase transition. The experimental testing is conducted to determine the material properties and validate the predicted results. Based on the predicted features of melt pools, the process efficiency maps that relate the printing productivity and the laser energy consumption efficiency to the process parameters are developed. The process parameters for SLS of the nanocomposite powders are then optimized through the process efficiency maps.

2. SLS process modeling

2.1. Heat transfer model

The physical phenomenon of SLS process is that the polymer powders are firstly melted under the laser irradiation and subsequently solidified in the cooling period. The temperature distribution and the fusion status in the first stage provide useful information for the optimization of process parameters. Therefore, this study focuses on the heat transfer during the sintering process.

The laser scanning process and the flow of relevant energy terms are illustrated in Fig. 1. The powder layer with a given thickness is paved on the sintered layers and then preheated to a temperature higher than the crystalline point for semi-crystalline polymers. As the laser beam scans on this layer, part of laser energy is absorbed, melting the powders and forming a melt pool. The temperature distribution and the dimensions of the melt pool such as the depth and width are important to evaluate whether the process parameters are appropriate.

A macroscopic modeling is used to analyze the heat transfer of SLS process, in which the powders are considered as continuum media with homogenized thermal and mechanical properties. The thermal equilibrium equation for heat transfer in a material with isotropic thermal properties is described by

$$\rho C\frac{\partial T}{\partial t} = \nabla\cdot(k\nabla T) + Q, \tag{1}$$

where ρ, C and k are the density, heat capacity and conductivity, respectively. Q is the volumetric heat input (W/m^3) from the laser power. The changes of these three material properties due to the solid-liquid phase transition should be considered in the simulation.

2.2. Heat source modeling

The required energy input for the fusion of the polymeric powders is induced by a 50 W CO_2 laser working at a wavelength of 10.6 μm. The laser energy was commonly modeled as a surface heat source with a Gaussian distribution on the powder bed. However, the interaction between the laser beam and powder bed is not considered.

When the laser beam irradiates on the powder bed, it experiences multiple reflections and absorption through the porous powders as illustrated in Fig. 2. The total energy is divided into three parts: reflected, absorbed and transmitted power. Only the absorbed part is used to melt powders. The laser energy can transmit into certain depth beneath the powder surface. Therefore, besides the energy distribution on the powder surface the heat transmission into the powder bed is also necessary to be considered in this modeling. As reported by Peyre et al. (2015), the Beer-Lambert attenuation law can be used to describe the laser transmission in the depth direction:

$$Q(x, y, z) = Q_0(x, y)\eta\exp(-\eta z), \tag{2}$$

where Q_0 is the heat distribution on the top surface (W/m^2) and η the extinction coefficient (m^{-1}) The term $\exp(-\eta z)$ represents the exponential decay of the laser power as a function of the depth from the top surface (Rombouts et al., 2005).

The heat flux distribution of Q_0 across the laser beam diameter is assumed to be a Gaussian relationship (Dong et al., 2009):

$$Q_0(x, y) = \frac{2AP}{\pi r_{\text{laser}}^2}\exp(-2\frac{x^2 + y^2}{r_{\text{laser}}^2}), \tag{3}$$

where P is the input laser power, A the power absorption coefficient and r_{laser} the laser radius. Through substituting Eq. (3) into Eq. (2), the volumetric heat source is modeled as

$$Q(x, y, z) = \frac{2AP}{\pi r_{\text{laser}}^2}\exp(-2\frac{x^2 + y^2}{r_{\text{laser}}^2})\eta\exp(-\eta z), \tag{4}$$

which satisfies the balance of total energy absorbed from the laser beam:

$$\int_0^{+\infty}\int_{-\infty}^{+\infty}\int_{-\infty}^{+\infty} Q(x, y, z)\mathrm{d}x\mathrm{d}y\mathrm{d}z = AP. \tag{5}$$

2.3. Boundary conditions

The powder layer paved on the sintered layers by the scraper or blade is preheated to the bed temperature T_b by the infrared radiant lights before the laser scanning. Therefore, the initial condition of the temperature at time $t = 0$ is applied as follows:

$$T(x, y, z, 0) = T_b. \tag{6}$$

During the laser sintering, the high energy laser beam scans and melts the polymeric powders in a very transient time. The energy absorbed from the laser heat is much greater than the energy released by the radiation (Bai et al., 2015). Therefore, the thermal radiation on the external surface is not considered in the thermal boundary condition as

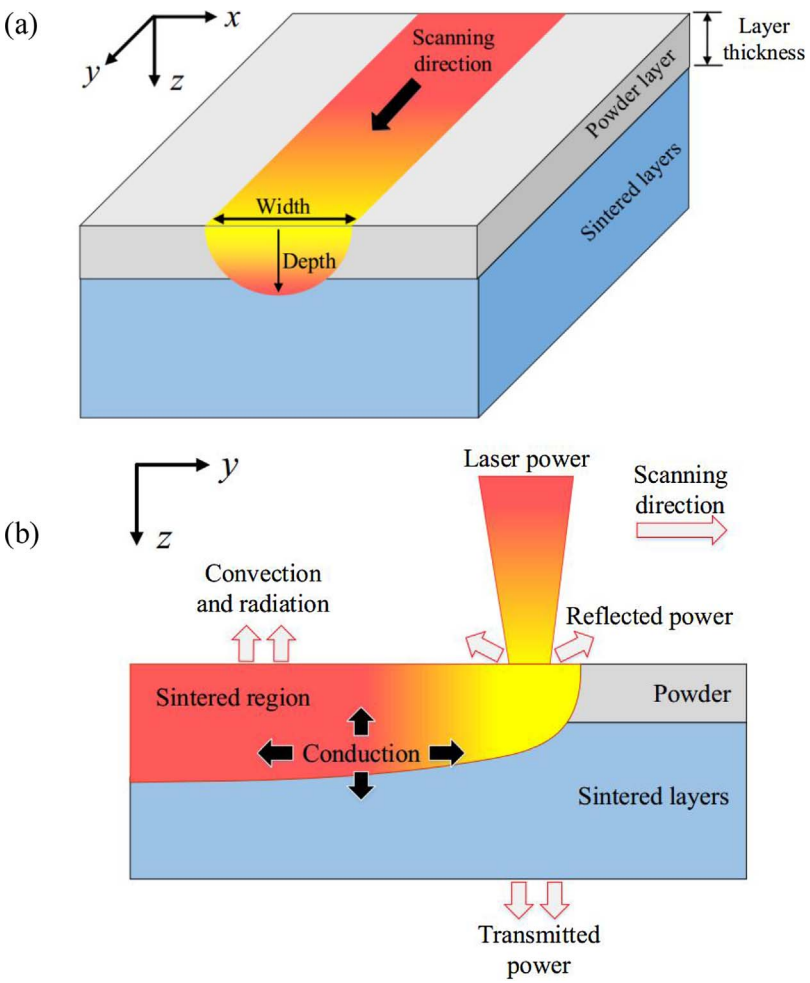

Fig. 1. Schematic of the laser scanning process: (a) overall view and (b) cross section view.

follows:

$$-nk\nabla T = q - h(T - T_b), \tag{7}$$

where n is the surface normal direction, q the surface heat input and h the natural convection coefficient.

3. Material properties and simulation cases

3.1. CNTs/PA12 composite

The material used in the SLS process is a nanocomposite prepared by coating CNTs on PA12 powder particles (PA2200 from EOS GmbH, Munich, Germany) with a weight fraction of 0.5%. The detailed preparation method was reported by Yuan et al. (2016a). The CNTs/PA12 powders exhibit a near-spherical shape with an average size of 60–70 μm. The capacities of the heat absorption and conduction are enhanced by the reinforcement of CNTs, which is beneficial to the sintering process.

3.2. Material properties

Several powder characterization techniques (Sutton et al., 2017) are

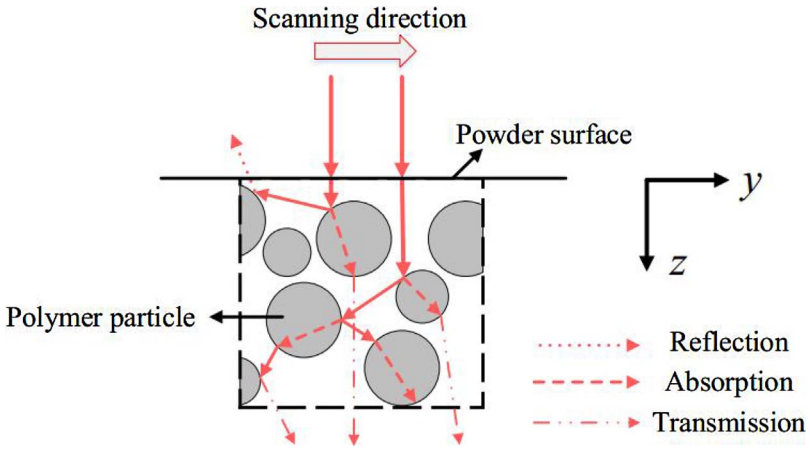

Fig. 2. Interaction between the laser and polymer particles (Laumer et al., 2016).

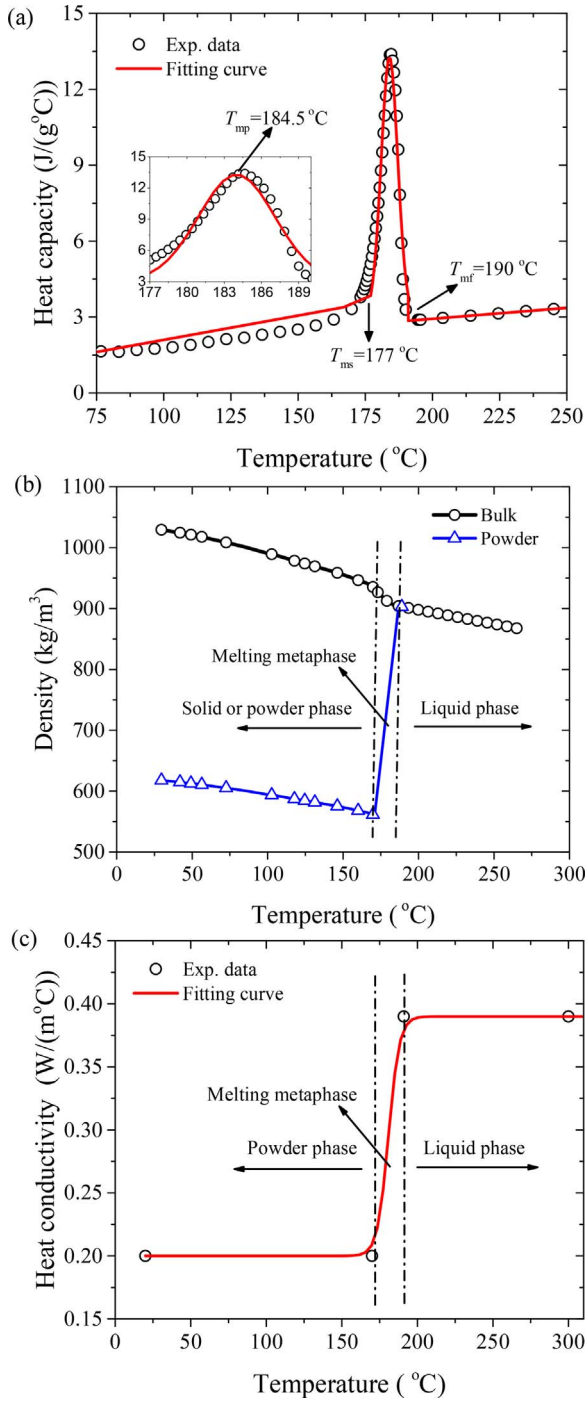

Fig. 3. Material properties of CNTs/PA12: (a) heat capacity, (b) density and (c) heat conductivity.

used to determine the temperature-dependent material properties of CNTs/PA12 from the powder to liquid phase. Differential scanning calorimetry (DSC) analysis is performed on a TA Instruments Q2000 to track the melting and solidification behavior of the powders. The onset and offset of the melting and recrystallization as well as the enthalpy change during the phase transition are obtained through a heating-cooling programming in DSC (Yuan et al., 2016b). The heat capacity as a function of the temperature is illustrated in Fig. 3(a). A slight increase occurs both in the powder and liquid phases. However, a significant hump is observed during the solid-liquid phase transition. A Gaussian function is used to describe the heat capacity (Peyre et al., 2015):

$$C(T) = C_m + \frac{\Delta H_m}{\sqrt{\pi(\Delta T_m/2)^2/2}} \exp\left(-\frac{2(T - T_{mp})^2}{(\Delta T_m/2)^2}\right),\ T_{ms} < T < T_{mf}, \tag{8}$$

where T_{ms} and T_{mf} represent the onset and offset of melting, respectively; $\Delta T_m = T_{mf} - T_{ms}$; T_{mp} is the temperature at the peak of the heat capacity; ΔH_m is the melting enthalpy; C_m is the heat capacity at the onset of melting.

The specific volume as a function of the temperature for the material in the heating process is measured through thermomechanical analyzer (TMA). The reciprocal of the specific volume is applied to evaluate the density as shown in Fig. 3(b). Due to the porosity in the powder bed, the density of powders is calculated as (Hussein et al., 2013)

$$\rho_{powder} = (1 - \phi)\rho_{solid}. \tag{9}$$

The porosity ϕ is assumed to vary from 0.44 at the powder phase to 0 at the liquid phase (Yuan et al., 2016b). During the melting metaphase, a linear increase of the density is applied in this study.

The heat conductivity of the material is also determined by DSC as shown in Fig. 3(c). A near step function is used to fit the experimental results (Riedlbauer et al., 2014):

$$k(T) = 0.2 + \frac{0.19}{1 + 10^{21.7 - 0.12T}}. \tag{10}$$

3.3. Simulation cases

Several cases with different process parameters listed in Table 1 are simulated with a scanning pattern commonly used in commercial printers as shown in Fig. 4. The ranges of these three process parameters are 10–40 W, 1000–4000 mm/s and 0.2–0.4 mm, respectively. The length and width of the powder layer are both 30 mm and its thickness is set as 0.1 mm for all the simulation cases. The thickness of the sintered layers is much larger than that of powder layer, which is set as 0.4 mm. The diameter of the laser beam is $\Phi = 0.42$ mm, which leads to $r_{laser} = 0.21$ mm (Bai et al., 2015). The material constants used in the simulations are listed in Table 2. The coating of CNTs enhances the heat absorption capacity of neat PA12 particles. Therefore, the power absorption coefficient used in this study is larger than that obtained in the experiments for neat PA12 powders (Laumer et al., 2016). It is also noted that the power extinction coefficient is assumed to be same as that of PA12 reported by Peyre et al. (2015). The other constants related to the heat capacity are determined through experimental testing.

4. Results and discussion

4.1. Experimental validation

The optical microscopy (Olympus DP72, Southborough, MA, USA) is

Table 1
Simulation cases with different process parameters.

Power P (W)	Speed s (mm/s)	Hatching space h (mm)
10	3000	0.2
10	4000	0.3
20	1000	0.3
20	3000	0.2
25	2000	0.2
25	3000	0.2
25	3000	0.3
25	3000	0.4
25	4000	0.2
30	1000	0.3
40	1000	0.2
40	4000	0.3

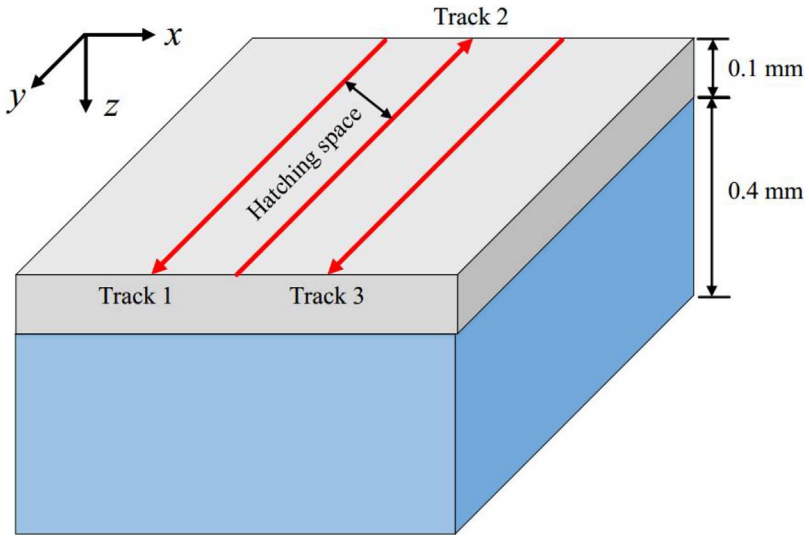

Fig. 4. Schematic view of the model with three scanning tracks in the powder layer.

Table 2
Material constants of CNTs/PA12.

Material constant	Value
Power absorption coefficient A	0.96
Extinction coefficient η (m^{-1})	9000 (Peyre et al., 2015)
Natural convection coefficient h (W/(m^2 °C))	25 (Bai et al., 2015)
Bed temperature T_b (°C)	174 (Yuan et al., 2016b)
Heat capacity at the onset of melting C_m (J/(g°C))	3.07
Melting enthalpy ΔH_m (J/g)	89.6
Temperature of fusion start T_{ms} (°C)	177
Temperature of the peak of heat capacity T_{mp} (°C)	184.5
Temperature of fusion finish T_{mf} (°C)	190

used to investigate the microstructures of the sintered cubic specimens, which are properly ground and polished to achieve smooth and reflective surfaces. Fig. 5(a) illustrates the microstructure on the x–z plane under the process parameters $P = 10$ W, $s = 3000$ mm/s and $h = 0.2$ mm and the predicted temperature distribution after the scanning of three tracks. The un-melted regions are observed in every layer due to the lack of fusion in the powder layer. The average fusion depth is around 70 μm which is smaller than the layer thickness. In the simulation result, the fusion zone where the temperature exceeds the melting point has the maximum depth of 82 μm, which is close to the experimental result.

While the laser power increases to 20 W, the powder layer is fully melted and thus the microstructure of the sintered specimen is more uniform as shown in Fig. 5(b). The depth of the fusion zone obtained in the simulation is 160 μm larger than the layer thickness and therefore some portions of the sintered layers are re-melted under the laser scanning. With the sounder microstructure, the specimen exhibits stronger mechanical performance (Yuan et al., 2016b). It is indicated that the full fusion of the powder layer should be satisfied in the optimization of process parameters.

4.2. Temperature distribution and melt pool

The process parameters affect the temperature history during the SLS process. Fig. 6 shows the heating-cooling-reheating behavior of a given material point on the powder surface under two sets of process parameters. It is noted that the material point is located at the first track and has a distance of 2.5 mm from the starting point of the scanning. As the laser beam passes through the material point during the first scanning, the temperature increases sharply to exceed the melting point, leading to the melting of powders, and afterwards gradually decreases. The temperature increase in the second track is attributed to the reheating induced by the laser even though the laser beam is offset by the hatching space 0.2 mm from the first track. Since the radius of laser beam is larger than the hatching space, part of heat flux is absorbed by the material point, leading to the increase of the temperature. However, the effect of the third scanning on the temperature is negligible because of the large distance (0.4 mm) between the third track and the material point at the first track.

The temperature distribution in the single track is determined by the laser power and scanning speed. The maximum temperature, the width and the depth of the melt pool all increase as the laser power increases and the scanning speed decreases. For the multi-track scanning, the hatching space controls the overlap of melt pools in the adjacent tracks, influencing the volume of the total melt pool. Furthermore, the hatching space affects the maximum temperature in the current scanning track due to the residual heat induced by the previous tracks. As shown in Fig. 7, the bottom of the melt pool after the three scanning has a wave shape in the simulation with a hatching space of 0.3 mm, which is different from the flat bottom for the case of 0.2 mm. The maximum temperature increases from 246 to 270 °C in the process under the smaller hatching space while no significant increment is observed under the larger one.

4.3. Process efficiency maps for parameter optimization

The simulation results of the temperature and the dimensions of melt pools are used to optimize the process parameters. The first constraint condition of the optimization is that the maximum temperature of melt pools T_{max} should be larger than the melting point but smaller than the upper limit of around 300 °C; i.e. $184.6 < T_{max} < 300$ °C. It is experimentally observed that the dimensional accuracy of the printed parts is difficult to control under the temperature higher than 300 °C because the powders near the boundary surfaces of the part may be also melted. The second constraint condition of the optimization is that the fusion depth d must be larger than the thickness of the powder layer and smaller than two times the thickness; i.e. $100 < d < 200$ μm. Otherwise, a lack of fusion or excess of the re-melted material will occur.

The objective of the process optimization is to maximize the process efficiency which includes both the printing productivity and the energy consumption efficiency. The printing productivity P_v is defined as the volume increment rate of the melt pool:

$$P_v = swd. \tag{11}$$

The energy consumption efficiency α is the ratio of the effective

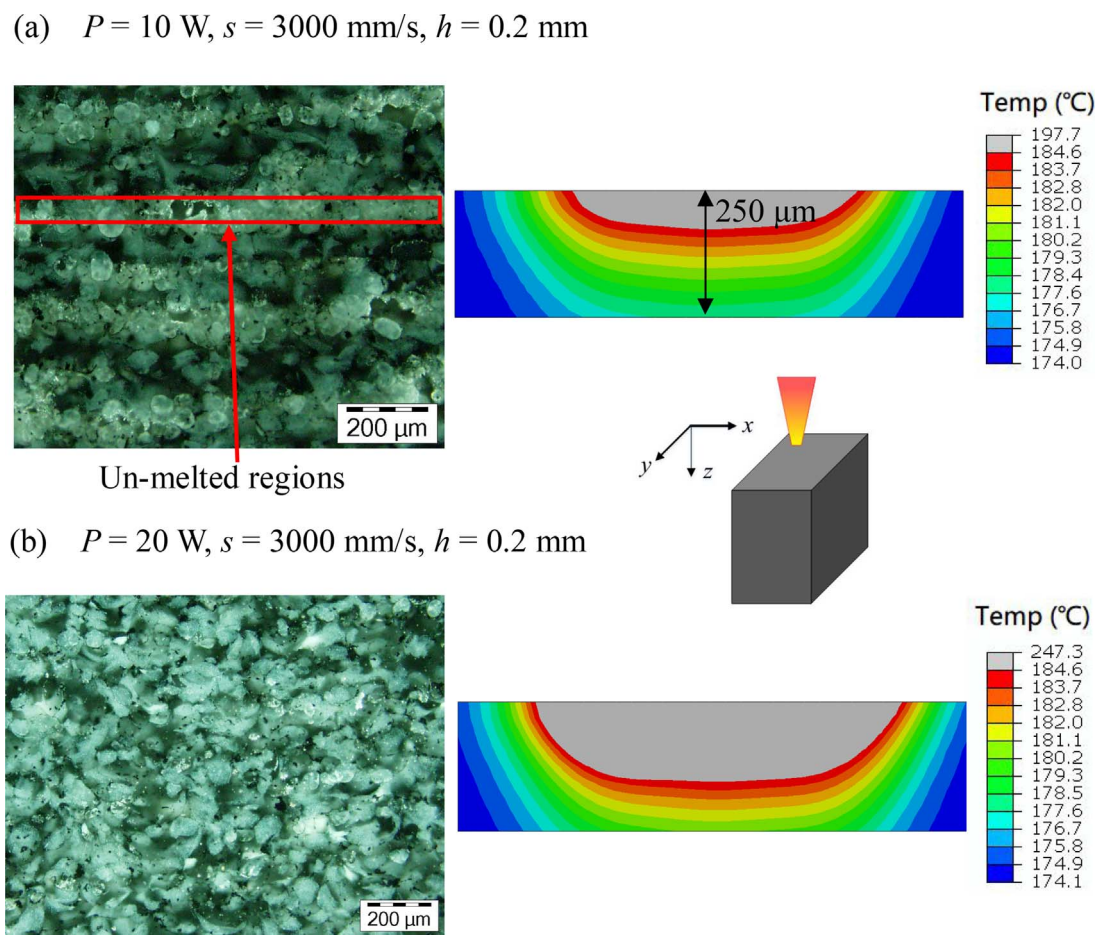

Fig. 5. Microstructures of the sintered specimen on the x–z plane and the fusion zones after the scanning of three tracks under the process parameters: (a) P = 10 W, s = 3000 mm/s and h = 0.2 mm; (b) P = 20 W, s = 3000 mm/s and h = 0.2 mm.

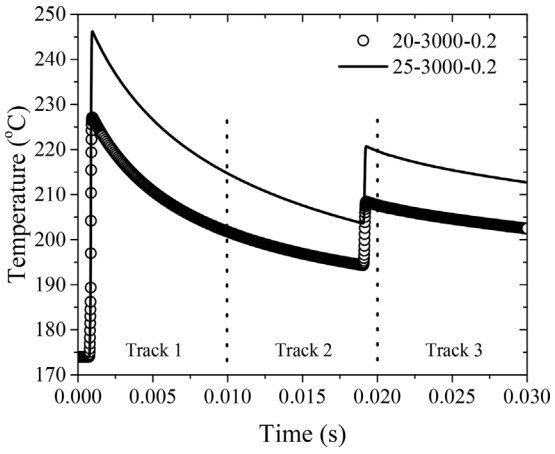

Fig. 6. Temperature history of the material on the powder surface during the laser scanning of three tracks under two sets of process parameters.

laser power used to form the melt pool to the total laser power input:

$$\alpha = \frac{P_v E_v}{P}, \tag{12}$$

where E_v is the energy required to melt the powders with unit volume. For the material CNTs/PA12, E_v = 0.064 J/mm^3 (Yuan et al., 2016b).

The laser power and the scanning speed are optimized through the results of the first track where the hatching space is not considered. Both parameters are usually combined together to describe the energy density on the irradiated area:

$$E_D = \frac{P}{s\Phi}. \tag{13}$$

As illustrated in Fig. 8(a), the relationship between the maximum temperature of the melt pool and the energy density is expressed via a linear function:

$$T_{max} = T_b + 3784.8E_D. \tag{14}$$

The width and depth of the melt pool as the functions of the energy density are shown in Fig. 8(b). Based on the theoretic solution of the heat transfer under the assumption of line heat source (Franco et al., 2010), the following equations are used to describe the dimensions:

$$w = 312\sqrt{\ln(168E_D)}$$
$$d = 206\sqrt{\ln(86.1E_D)}. \tag{15}$$

Based on above three equations, the maximum temperature and the fusion depth of the melt pool can be obtained by the laser power and scanning speed. Fig. 9(a) shows the available regions of both parameters determined by the constraint conditions. The parameters should be optimized in the overlapped region with boundaries marked by two red lines. It is also found that the energy density level is suggested in the range of 0.015–0.04 J/mm^2. Under the low power and high speed, the laser energy is not enough to melt the whole powder layer, while the fusion depth is too large under the condition of the high power and slow speed.

The optimization objective is determined by substituting Eqs. (13) and (15) into Eqs. (11) and (12). Fig. 9(b) illustrates the contour map of the printing productivity P_v which increases to its maximum value as the parameters approach to the right upper corner of parameter ranges.

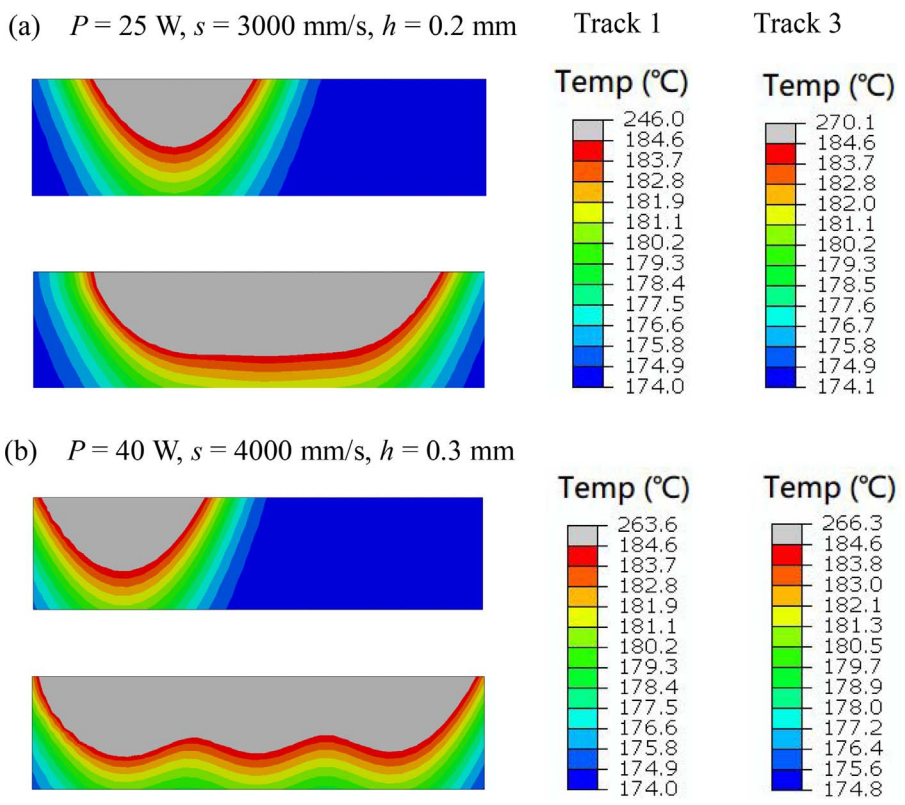

Fig. 7. Evolution of melt pools in the scanning of three tracks under two sets of process parameters.

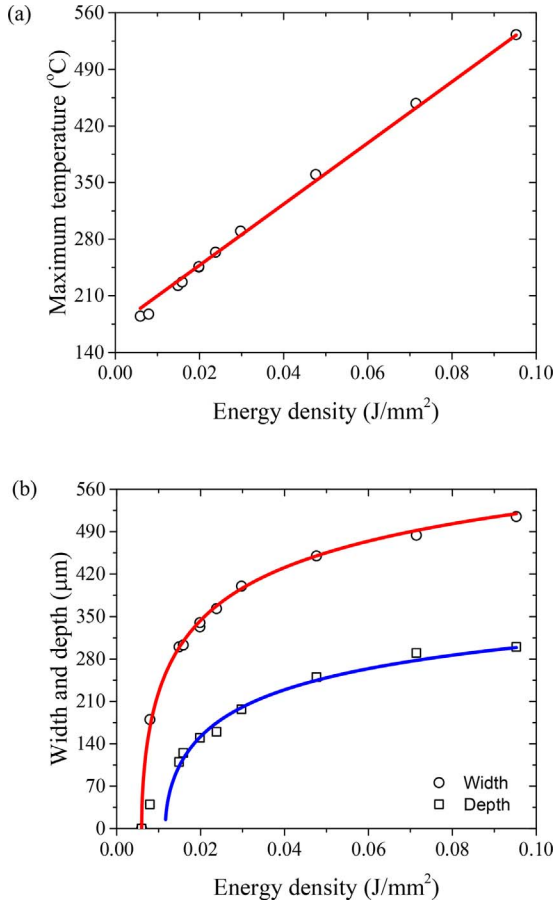

Fig. 8. Evolutions of (a) the maximum temperature and (b) the width and depth of melt pool as a function of the energy density in the first track.

The maximum value around 256 mm^3/s occurs under the parameters $P = 40$ W and $s = 3800$ mm/s, which falls in the available region for the parameter selection as shown in Fig. 9(a). The scanning speed is dominant in controlling the productivity compared to the laser power. Under the high speed, the power needs to be large in order to create the melt pool with enough fusion depth. Fig. 9(c) depicts the contour map of the energy consumption efficiency α. The cross lines in the available region for the parameter selection are omitted to make the map clear. The maximum efficiency is around 0.42, indicating that the majority energy is wasted in heating the powders outside the melt pool and increasing the temperature of the melted material. Therefore, too high temperature in the melt pool decreases the efficiency of power use, besides there is high risk of the material degradation. With the consideration of both terms of the optimization objective, the optimized process parameters are obtained as $P = 40$ W and $s = 3800$ mm/s.

The hatching space is determined by evaluating the predicted shape of the melt pool. As shown in Fig. 7, the overlap of two adjacent tracks is favorable to achieve high process efficiency under the case of hatching space of 0.3 mm. Furthermore, the maximum temperature in each track is very stable, which is beneficial to the printing process. Therefore, the optimized parameters for SLS process of the material CNTs/PA12 are obtained as $P = 40$ W, $s = 3800$ mm/s and $h = 0.3$ mm.

5. Conclusions

The process efficiency for SLS of polymeric composite powders is investigated via numerical modeling and experimental testing. The process modeling is conducted to evaluate and predict the temperature distribution and the dimensions of melt pools during the sintering of PA12/CNTs nanocomposite. The interaction between the laser beam and power bed is considered in the model of laser heat source. The temperature-dependent material properties from the solid to liquid phase are determined through the experimental testing. The predicted fusion depths under different process parameters are validated against

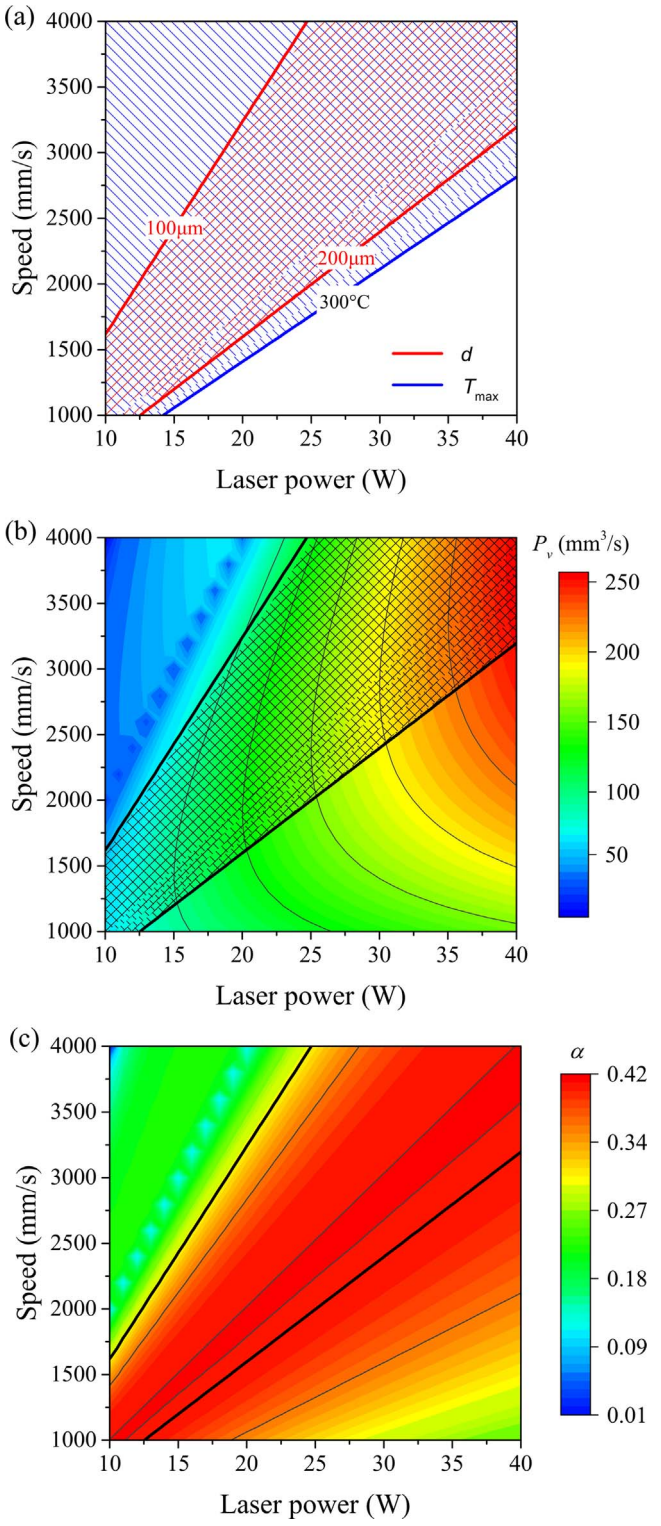

Fig. 9. Contour maps of (a) the available regions determined by two constraint conditions, (b) the process productivity and (c) the energy consumption efficiency in the parameter ranges of 10–40 W and 1000–4000 mm/s.

the experimental results.

Based on the predicted results, the maps that relate the printing productivity and the laser energy consumption efficiency to the process parameters are established through the use of energy density. The optimization of the process parameters is conducted through the maps under the necessary constraint conditions on the maximum temperature and the fusion depth of melt pools. It is found that the energy density level is suggested in the range of 0.015–0.04 J/mm^2. The optimized parameters for SLS process of the material CNTs/PA12 are obtained as P = 40 W, s = 3800 mm/s and h = 0.3 mm.

Acknowledgment

The authors would like to acknowledge the financial supports from the National Research Foundation Medium Sized Center, Singapore through the Marine and Offshore Program and the Ministry of Education, Singapore (Academic Research Fund TIER 1 RG174/15).

References

Bai, J., Goodridge, R.D., Yuan, S., Zhou, K., Chua, C.K., Wei, J., 2015. Thermal influence of CNT on the polyamide 12 nanocomposite for selective laser sintering. Molecules 20, 19041–19050.

Bai, J., Yuan, S., Shen, F., Zhang, B., Chua, C.K., Zhou, K., Wei, J., 2017. Toughening of polyamide 11 with carbon nanotubes for additive manufacturing. Virtual Phys. Prototyp. 1–6.

Caulfield, B., McHugh, P.E., Lohfeld, S., 2007. Dependence of mechanical properties of polyamide components on build parameters in the SLS process. J. Mater. Process. Technol. 182, 477–488.

Dong, L., Makradi, A., Ahzi, S., Remond, Y., 2009. Three-dimensional transient finite element analysis of the selective laser sintering process. J. Mater. Process. Technol. 209, 700–706.

Fatemi, S., Ashany, J.Z., Aghchai, A.J., Abolghasemi, A., 2017. Experimental investigation of process parameters on layer thickness and density in direct metal laser sintering: a response surface methodology approach. Virtual Phys. Prototyp. 12, 133–140.

Foroozmehr, A., Badrossamay, M., Foroozmehr, E., Golabi, S., 2016. Finite element simulation of selective laser melting process considering optical penetration depth of laser in powder bed. Mater. Des. 89, 255–263.

Franco, A., Romoli, L., 2012. Characterization of laser energy consumption in sintering of polymer based powders. J. Mater. Process. Technol. 212, 917–926.

Franco, A., Lanzetta, M., Romoli, L., 2010. Experimental analysis of selective laser sintering of polyamide powders: an energy perspective. J. Clean. Prod. 18, 1722–1730.

Goodridge, R.D., Tuck, C.J., Hague, R.J.M., 2012. Laser sintering of polyamides and other polymers. Prog. Mater. Sci. 57, 229–267.

Hussein, A., Hao, L., Yan, C.Z., Everson, R., 2013. Finite element simulation of the temperature and stress fields in single layers built without-support in selective laser melting. Mater. Des. 52, 638–647.

Körner, C., Attar, E., Heinl, P., 2011. Mesoscopic simulation of selective beam melting processes. J. Mater. Process. Technol. 211, 978–987.

Körner, C., Bauereiß, A., Attar, E., 2013. Fundamental consolidation mechanisms during selective beam melting of powders. Modell. Simul. Mater. Sci. Eng. 21, 085011.

Khairallah, S.A., Anderson, A., 2014. Mesoscopic simulation model of selective laser melting of stainless steel powder. J. Mater. Process. Technol. 214, 2627–2636.

Laumer, T., Stichel, T., Nagulin, K., Schmidt, M., 2016. Optical analysis of polymer powder materials for Selective Laser Sintering. Polym. Test. 56, 207–213.

Peyre, P., Rouchausse, Y., Defauchy, D., Régnier, G., 2015. Experimental and numerical analysis of the selective laser sintering (SLS) of PA12 and PEKK semi-crystalline polymers. J. Mater. Process. Technol. 225, 326–336.

Riedlbauer, D., Drexler, M., Drummer, D., Steinmann, P., Mergheim, J., 2014. Modelling, simulation and experimental validation of heat transfer in selective laser melting of the polymeric material PA12. Comp. Mater. Sci. 93, 239–248.

Rombouts, M., Froyen, L., Gusarov, A.V., Bentefour, E.H., Glorieux, C., 2005. Light extinction in metallic powder beds: correlation with powder structure. J. Appl. Phys. 98, 013533.

Sachdeva, A., Singh, S., Sharma, V.S., 2013. Investigating surface roughness of parts produced by SLS process. Int. J. Adv. Manuf. Technol. 64, 1505–1516.

Singh, S., Sachdeva, A., Sharma, V.S., 2017. Optimization of selective laser sintering process parameters to achieve the maximum density and hardness in polyamide parts. Prog. Addit. Manuf. 2, 19–30.

Sutton, A.T., Kriewall, C.S., Leu, M.C., Newkirk, J.W., 2017. Powder characterisation techniques and effects of powder characteristics on part properties in powder-bed fusion processes. Virtual Phys. Prototyp. 12, 3–29.

Tan, W.S., Chua, C.K., Chong, T.H., Fane, A.G., Jia, A., 2016. 3D printing by selective laser sintering of polypropylene feed channel spacers for spiral wound membrane modules for the water industry. Virtual Phys. Prototyp. 11, 151–158.

Wang, R.J., Wang, L.L., Zhao, L.H., Liu, Z.J., 2007. Influence of process parameters on part shrinkage in SLS. Int. J. Adv. Manuf. Technol. 33, 498–504.

Yadollahi, A., Shamsaei, N., 2017. Additive manufacturing of fatigue resistant materials: challenges and opportunities. Int. J. Fatigue 98, 14–31.

Yuan, S.Q., Bai, J.M., Chua, C.K., Wei, J., Zhou, K., 2016a. Highly enhanced thermal conductivity of thermoplastic nanocomposites with a low mass fraction of MWCNTs by a facilitated latex approach. Compos. Pt. A-Appl. Sci. Manuf. 90, 699–710.

Yuan, S.Q., Bai, J.M., Chua, C.K., Wei, J., Zhou, K., 2016b. Material evaluation and process optimization of CNT-coated polymer powders for selective laser sintering. Polymers 8, 370.